Early flame propagation in a spark-ignition engine measured with quasi 4D-diagnostics

Early flame propagation in a spark-ignition engine measured with quasi 4D-diagnostics

B. Peterson[1], E. Baum[1], B. Böhm[2], A. Dreizler[1]

[1]Fachgebiet Reaktive Strömungen und Messtechnik (RSM), Center of Smart Interfaces (CSI), Technische Universität Darmstadt, Jovanka-Bontschits-Straße 2, 64287 Darmstadt, Germany

[2]Fachgebiet Energie und Kraftwerkstechnik (EKT), Technische Universität Darmstadt, Jovanka-Bontschits-Straße 2, 64287 Darmstadt, Germany

Corresponding author: Brian Peterson, Jovanka-Bontschits-Straße 2, 64287 Darmstadt, Germany, Fax: +49 6151 16 6555, E-mail: peterson@csi.tu-darmstadt.de

Colloquium: Diagnostics

Paper length

- Main text (Introduction to Acknowledgements): 4224
- Equations: (1+2)x7.6=23
- Nomenclature: N/A
- References: (32+2)x2.3x7.6=594
- Tables:
  - Tab. 1: (8+2)x7.6=76
- Figures & figure captions:
  - Fig. 1: (39+10)x2.2+7= 115
  - Fig. 2: (35+10)x2.2+8=107
  - Fig. 3: (40+10)x2.2x2+45=265
  - Fig. 4: (82+10)x2.2+31=233
  - Fig. 5: (95.5+10)x2.2+38=270
  - Fig. 6: (97+10)x2.2+55=290
  - Total figures: 1280

Total count: 6197<6200

Abstract

This paper presents the first results towards experimentally resolving the local three-dimensional (3D) flame propagation and turbulence-chemistry-interaction in a spark-ignition engine using temporally resolved multi-planar laser diagnostics. The experimental method utilizes simultaneous dual-plane laser induced fluorescence (LIF) of OH and stereoscopic PIV (SPIV) to locally resolve 3D flame displacement speed during the early flame development when less than 5% of the mass has been consumed. OH-LIF is used to track the reaction-zone position and flame normal direction in 3D space, while SPIV measures the convection of the identified flame contours. Based on the vectorial difference of the 3D convection and absolute propagation of the reaction-zone, the 3D displacement speed (s_T) is calculated. An instantaneous flame realization shows a large dynamic range of local s_T and local flow transport, while also revealing the importance to resolve these quantities in 3D. Several flame-flow configurations are shown along the flame surface and each uniquely defined the local flame transport along the individual flame realization. A detailed uncertainty and sensitivity analysis is performed, confirming the validity of the s_T distribution resolved for the methodology and operating conditions. A discussion on the different mechanisms leading to the large distribution of s_T for the given operations is included and testifies to complex nature of the in-cylinder flame development in this early stage. The limitations of the presented methodology are discussed particularly in the need for improved spatial resolution and additional volumetric information. The merits and limitations of the presented work provides an improved understanding of what is further needed to better resolve local 3D flame transport in engines for both experimental and numerical methodologies.

Keywords: Multi-plane imaging; laser induced fluorescence; stereoscopic PIV; flame displacement speed; spark-ignition engine

Early flame propagation in a spark-ignition engine measured with quasi 4D-diagnostics

B. Peterson, E. Baum, B. Böhm, A. Dreizler

1. Introduction

A detailed understanding of local flame propagation in spark-ignition (SI) engines is required to further improve combustion performance, realize next-generation combustion strategies, and provide valuable data to build predictive models in turbulent combustion. Flame-front progression within premixed systems is primarily governed from two components: (1) unburned-gas advection and (2) flame-normal displacement speed [1]. The latter has been recognized as one of the most important flame properties [2] particularly regarding numerical models using flame surface density (FSD) [3] and level-set [4] approaches, where such local effects must be included into sub-grid scale models [2,5]. In SI engines, like most turbulent combustion environments, flow-direction and flame-geometry are highly three-dimensional (3D). Determination of the flame-normal displacement speed and advection velocity within a 3D domain is necessary to appropriately resolve local displacement speeds in turbulent combustion.

Laser-based diagnostic techniques provide non-intrusive measurements of leading scalar and vector properties that quantify fundamental processes in combustion systems. With regards to flame propagation, traditional methods such as Schlieren, chemiluminescence, Mie scattering, and laser induced fluorescence (LIF) have measured integral flame growth rates for spherical-based flame geometries, which have provided the basis for most combustion models in practical systems [6-13]. A more comprehensive understanding of flame propagation however, has come from multi-parameter diagnostics that utilize multi-planar measurements to resolve coupling between turbulent flow and reaction chemistry. Measurements employing such techniques have provided detailed statistics of the 3D flame-normal, flame stretch, advection velocity, and local 3D displacement speeds in turbulent

combustion [5,14-17]. Sophisticated, well-designed diagnostic methods are considered high-priority for an improved understanding in turbulent combustion.

Within SI engines, experimental efforts have primarily resolved integral flame growth rates from single-plane imaging, line-of-sight, and optical-fiber probes [9,11,12,18]. Local 2D flame displacement speeds have been resolved utilizing high-speed laser tomography and particle image velocimetry (PIV) in a boosted optical SI engine [19]. Using short laser-pulse separation, Mie scattering images resolved planar flame displacement, while local advection velocities were obtained from PIV. Although these measurements provided valuable classification of turbulent premixed flames within engines, the assumption of 2D flame propagation biases displacement speed calculations [15] and resolving the 3D flame-normal and flow velocity must be considered.

This work utilizes the dual-plane OH-LIF, stereoscopic PIV (SPIV) methodology from [14] to resolve local 3D displacements speeds in an optical SI engine. The engine is operated at 800RPM with stoichiometric, premixed isooctane-air mixtures. Images were acquired during the early-flame development when less than 5% of the mixture is consumed, typically regarded as the crucial stage of flame development defining subsequent combustion [20]. Measurements reveal individual contributions of local flow velocity and flame displacement speed on the overall transport of the flame surface. A detailed uncertainty and parameter sensitivity analysis is presented to discuss the validity of the results and limitations of the measurements.

2. Experimental Setup

2.1 Engine

Experiments were performed in a single-cylinder optical SI engine [21]. The engine was operated at 800RPM with port-fuel injection of isooctane (27.4mg/cycle) to provide a stoichiometric, homogeneous mixture. The operating conditions shown in Table 1 are chosen to mimic low-load, idle engine operation. Low-load operation is technically relevant as it can be prone to combustion instabilities [20]. Moreover, the operating conditions provided low turbulence levels ($u' \sim$1m/s (Reynolds decomposition) not shown) and repeatable thermodynamic conditions for reliable measurements of local flame propagation.

The fuel-air mixture was ignited by a spark plug (NGK Spark Plug Co., Ltd.) with dwell of 3.5ms. Spark timing, ST=19 crank-angle degrees (CA^{o}) before top-dead-center (bTDC), was chosen to optimize indicated mean effective pressure (IMEP) and combustion stability (COV of IMEP <2%). The engine was fired 200 cycles before acquiring measurements and provided stable engine boundary conditions.

2.2. Diagnostics

The optical setup is similar to that used in [14] and shown in Fig. 1. A frequency-doubled Nd:YAG dual-cavity laser (Edgewave, INNOSLAB IS4 II-DE, 532nm) operating at 4.8kHz was used for SPIV measurements. Laser light passed through focusing optics to provide a laser sheet (0.5mm thickness), which was centered vertically within the tumble plane and bisected the spark plug center electrode. Two CMOS cameras (Phantom V.711, double-frame exposure) in Scheimpflug arrangement placed on each side of the engine imaged Mie scattering off chemically inert boron nitride (BN) particles (0.5µm diameter), which were seeded into the intake flow. The cameras were mounted α=14° off-normal to the LIF cameras and imaged a 15x25mm^2 region centered around the spark plug.

The combustion radical hydroxyl (OH) was imaged simultaneously in two parallel, vertical planes by two independent double-pulsed UV laser systems. Each laser system used a frequency-doubled dye laser (Sirah, Precision Scan, Rhodamine 6G) pumped by a double-pulsed Nd:YAG laser (Spectra Physics, PIV400, 532nm) each providing two UV laser pulses (24mJ/pulse) temporally separated by Δt_{LIF}. The dye lasers were tuned to 282.9nm to excite the $Q_1(6)$ line of the A-X(1-0) transition of OH.

The laser beams from each UV laser system were sent through independent focusing optics and spatially separated to provide two parallel UV light sheets (0.2mm thickness) offset by $\Delta z=\pm 0.5$mm on each side of the PIV light sheet (Fig. 1). Experiments were also conducted with $\Delta z=\pm 0.25$ and ± 0.75mm. The sheet separation and thickness was adjusted by UV-sensitive beam-monitor (DataRay). Fluorescence emission from each laser sheet passed through high-transmission, band-pass filter (Laser Components, UV-B) and was imaged onto two separate image intensifiers (LaVision, High-speed IRO) coupled to 14-bit CCD cameras (LaVision, ImagerProX, double-frame exposure) arranged on each side of the engine. Spontaneous OH* chemiluminescence and flame luminosity were suppressed by gating each intensifier to 300ns. The projected *pixel* resolution of both LIF detection systems was 20μm, while the *spatial* resolution was 80μm determined by a Siemens-stern (contrast transfer function).

Integral flame growth was imaged by chemiluminescence. An unintensified CMOS camera (LaVision, HSS5, 10bit) operated at 5kHz and imaged onto a 40x55mm^2 area through the piston via the crank-case mirror. Two identical long-pass 550nm filters (CVI) were used to suppress 532nm laser light.

An optical crank-angle encoder (AVL) was used to synchronize all lasers and cameras to the engine. The LIF systems were synchronized by a programmable timing unit (LaVision, PTU) to provide images at a fixed CA^o. Each double-pulsed LIF system operated at 10Hz providing two temporally resolved LIF images (t_0, $t_0+\Delta t_{LIF}$) in each plane at 14°bTDC (i.e. 5 CA^o after spark), when the flame has consumed less than 5% of the mixture. The UV laser pulses between each laser system were offset by 400ns to avoid cross talk

between the LIF images in each plane. PIV lasers and cameras operated at 4.8kHz to measure the three-component (3C, *u,v,w*) velocity from 20°–2° bTDC. The first PIV laser pulse was triggered 12.5µs after the first UV pulse and the pulse separation for the PIV (Δt_{PIV}) was 25µs, while the pulse separation for each LIF laser system (Δt_{LIF}) was 50µs. LIF images were recorded every other cycle for a 200 cycle sequence, while PIV images were recorded for 200 consecutive cycles. Chemiluminescence images started 1 CA^{o} before spark and recorded 20 images/cycle at 5kHz for 200 consecutive cycles.

2.3 Data Processing and flame speed calculation

The absolute velocity of the reaction-zone (w) is defined as sum of the local unburned convection velocity (u) and the flame displacement speed (s_T) relative to the flow in the flame-normal direction (n). This is shown schematically in Fig. 2 and Eq. (1).

$$w = u + n \cdot s_T \qquad (1)$$

The image processing procedure presented in [14] was used for the reconstruction of the flame surface onto the SPIV plane and to extract s_T from the acquired images. The reaction-zone was identified in the LIF images by applying a non-linear diffusion filter [22] based on anisotropic operating splitting in combination with a Canny edge-detection algorithm. The identified reaction-zone is superimposed onto a raw LIF image in Fig. 3a. The red dashed line highlights a region of high in-plane curvature towards the products, which is not resolved due to weak LIF gradients. Although such areas represent <5% of the overall detected contour, systematic errors in s_T will occur in such regions.

A NURBS spline interpolation [23] was used to construct the 3D surface between the flame contours identified in each OH-plane and a patch diffusion algorithm [24] removed numerical noise from the constructed surface. The 3D flame surface is projected through the SPIV-plane providing the local flame-normal at z=0mm. The convection velocity (u) was extracted 0.4mm in front of the flame surface (flame-

normal direction) on the SPIV-plane at t_0. 1D laminar flamelet simulations [25] demonstrated this distance is sufficient to avoid effects of pre-heating and expansion.

The 3D displacement speed was determined by transporting the position of the reaction-zone at t_0, z=0mm by the local 3C velocity in 3D space. The remaining distance between the transported contour and the nearest point on the reconstructed flame surface at time $t_0+\Delta t_{LIF}$ in the flame-normal (n) is representative of the local displacement speed s_T. Local values were determined for individual points spaced 20μm (i.e. projected LIF pixel size) along the flame contour on the SPIV plane. The limited *spatial* resolution (80μm LIF, 400μm SPIV) is greater than the laminar (thermal) flame thickness ($\delta_L \approx 45\mu m$, from 1D flamelet simulation). The detected flame front in the measurements is therefore recognized as a spatially filtered quantity. As a clear separation from previous work [2,14,15,26,27,28], which use various methodologies to assess the local *laminar burning velocity*, all results here are based on a filtered displacement speed (s_T), referred to as *turbulent displacement speed.*

SPIV images were processed with a commercial software (LaVision DaVis 8.1). Spatial calibration and dewarping of the PIV images were accomplished with a 3D target (LaVision, Type7). Self-calibration was accomplished from 200 Mie scattering images and provided a remaining average pixel disparity <0.01 pixels. Image cross-correlation and vector calculation were performed with a decreasing window size multi-pass algorithm. Final interrogation window size was 16x16 with 75% overlap providing 0.1mm vector spacing.

The integral flame growth rate (from chemiluminescence) was calculated assuming spherical flame growth [29]. Burned and unburned gas densities to determine the integral growth rate were resolved from 1D flamelet calculations.

3. 3D flame surface and local displacement speed realization

This section presents a single realization describing the flame propagation with respect to local 3D flame-orientation, convection velocity, and 3D displacement speed. A statistical distribution of s_T is shown and further discussed in sections 4 and 5.

The reconstructed 3D flame surface projected onto the 2D3C flow-field is shown in Fig. 3b and provides an overview of the flame development for an individual cycle. The red and blue contour lines represent the reaction-zones in the z=0.5mm and -0.5mm OH-LIF planes, respectively. The gray surface depicts the reconstructed 3D flame surface between the LIF contours and the white contour is the flame position on the SPIV plane. A side-view of the 3D flame surface (Fig. 3c) further reveals the flame geometry within the 3D domain. Velocity vectors (every 4^{th} vector) represent the local 3C velocity within the burned and unburned regions. The color-scale corresponds to the 3C velocity magnitude. The rectangles (white dashed lines 1 and 2) highlight flame segments discussed in Fig. 4.

The flame surface shown in Fig. 3b surrounds the spark plug electrodes and is approximately 35mm in length. Both in-plane and out-of-plane wrinkling is evident for the reconstructed flame surface and is discussed further within section 4. The flow to the left of the flame exhibits high velocities (8-10m/s) directed towards reactants, resulting in strong transport of the flame surface. To the right of the flame, velocity magnitude is significantly lower (1-4 m/s) and primarily directed opposing the flame surface.

Figure 4 shows enlarged views of two selected flame segments (regions 1 and 2 in Fig. 3b) to describe the flame transport of the instantaneous flame realization. Top images show the 3D flame surfaces at time t_0 and $t_0+\Delta t_{LIF}$ (denoted as flame surface 1 (FS1) and flame surface 2 (FS2), respectively) with respect to the burned and unburned regions. Middle images show the convection of the 2D flame contour identified on the SPIV plane. Bottom images show local s_T values superimposed onto FS1.

Flame segment 1 (first-column) exhibits high convection velocities (8-10m/s), which enhances flame transport toward the reactants. s_T values (-1 to 3m/s) are much lower than convection velocities along

the flame segment. A negative s_T value occurs when the convected contour (black line) is transported further than FS2, resulting in a flame-normal direction toward the products rather than the reactants. The occurrence of negative s_T for all cycles is discussed in section 5. Flame segment 2 (second column) shows that the convection velocity opposes the flame surface and transports the flame toward the products, while s_T transports the flame in the direction of reactants. Since the convection velocity (4-5 m/s) is greater than s_T (2-4 m/s) the flame surface recedes toward the products and overall transport is small.

Local s_T (blue) and convection velocities (black) along the entire flame surface are shown in Fig. 5a (every 4th vector). Velocity values as well as out-of-plane convection- and flame-angle (β, Fig. 1) are shown along the flame contour in Fig. 5b,c. Contour points in Fig. 5b,c begin at the top, left position of the flame contour and walk along the flame in equally spaced points (1250 total points). Shaded regions highlight the flame segments in Fig. 4 and the red line reveals the ensemble-average displacement speed (2.6m/s) along the flame surface. Both local s_T and convection velocity exhibit a large dynamic range ($-3 \leq s_T \leq 10$m/s; $0 \leq u \leq 10$m/s) and are non-uniformly distributed along the flame surface. Furthermore, both the flame and flow velocity exhibit a strong out-of-plane orientation. Along the flame surface many flame-flow configurations can be observed. On the left-side of the image, the flame exhibits strong convection velocities towards reactants with a large range of s_T, leading to strong transport of the flame. Near the bottom, the flame approaches the piston (y=-5mm) and the flame-normal is perpendicular to the unburned gas velocity. To the right, unburned-gas velocity opposes the flame-normal, leading to lower flame transport. The individual flame realization reveals the complex nature of flame transport in the engine.

The distribution of s_T along the flame surface for 80 cycles is shown as bars in Fig. 6. It reveals that s_T covers a broad range of values ranging from -5 to 15m/s, with mean value $\bar{s}_T$ =2.6m/s. Discussion of this range is presented within the following sections.

4. Uncertainty and Sensitivity Analysis

Calculation of s_T is based on the precision of each input parameter in eq. 1 as well as the quality of the linear approximation of the 3D flame surface. Discussion of measurement uncertainty (accuracy, precision) and parameter sensitivity is considered within this section.

Accuracy of the calculated s_T is assessed in comparison to integral flame growth rate obtained from chemiluminescence imaging [29]. Chemiluminescence images depicting the integral growth rate (not shown) provide a spherical global flame growth of 2.1±1.2m/s at the same CA^o (statistic from 80 cycles). This is in good agreement with $\bar{s}_T$.

Precision of local s_T values arise from the precision of each input parameter, namely reaction-zone identification and unburned gas velocity. Each LIF-detection system had a *spatial* resolution of 80μm. This could provide a maximum possible offset of 160μm between FS1 and FS2. Assuming the LIF-detection within this offset is Gaussian distributed, a reasonable offset between flame surfaces is 53μm (i.e. 1σ), providing an uncertainty ±1.1m/s, while the *maximum* offset provides ±3.1m/s. SPIV measurements have an estimated precision of 10% from [30] corresponding to a *maximum* uncertainty of 1m/s. A root mean square estimation for s_T provides a 1σ uncertainty of ±1.5m/s, or *maximum* (3σ) of ±4.5m/s.

The calculation of s_T is also based on several limitations of the measurement systems. It is anticipated that flow and flame detection is under-resolved in regards to fine-scale structures that exist in turbulent flows [4]. Furthermore, the linear interpolation of the 3D flame surface and laser sheet separation (Δz)

provides limited out-of-plane resolution. Therefore it is necessary to address the sensitivity of system parameters on the calculation of s_T. As depicted in Fig. 3a not all regions of the flame are resolved. However, this consists of less than 5% of the flame contour for all cycles reported. The low occurrence of these areas will not significantly affect the s_T distribution and is therefore not included in this analysis. The following sensitivity analysis discussion is *separate* from the s_T uncertainty values already reported.

SPIV was processed with a 16x16 pixel window size and data processing was repeated for a 32x32 pixel window to assess the sensitivity of SPIV resolution for s_T. s_T was compared at each location for both processed datasets and Δs_T is the local difference. This resulted in an average Δs_T=0.7m/s and did not significantly alter the s_T distribution (red line, Fig. 6a). The extraction location of the unburned convection velocity was also varied (0.1-0.6mm, 0.1mm increments) for the 16x16 pixel window size dataset to assess the sensitivity of flow location in the flame-normal. The average Δs_T is 0.8m/s and reveals a similar s_T distribution (not shown for clarity).

Experiments were repeated with Δz=0 mm to assess differences of the detected flame contour imposed from the processing methods and different LIF-detection systems. An average deviation between detected flame contours was 120μm, which will produce an artificial normal flame-angle of $\beta\pm12^o$. Displacement speed calculations were repeated with $\beta\pm12^o$ and revealed a maximum Δs_T of 0.4m/s. Additional experiments were repeated with Δz=0.25 and 0.75mm to assess the sensitivity of Δz. This revealed similar s_T distributions as Δz=0.5mm (Fig. 6a black and blue lines vs. bars). In-plane flame curvature revealed a statistic of κ=-0.2$\pm$0.8mm^{-1} from the 80-cycle distribution. Assuming that out-of-plane curvature is similar to in-plane curvature, the linear reconstruction method for Δz =0.25 and 0.5mm is argued valid to capture the 3D flame structure and assumed that sub-wrinkling not captured by the linear reconstruction is minimal.

Out-of-plane convection and flame orientation can still bias the multi-planar measurements. Therefore, results were conditionally sampled to only include measurements that exhibited an out-of-plane convection angle $|\beta|<45^{o}$ and out-of-plane convection velocity $|w|$<2m/s. Although 40% of the measurement data was removed, the s_T distribution remained nearly the same (Fig. 6b, red and black lines vs. bars). Results were further conditionally sampled to include data that exhibited absolute displacement speeds w>2m/s (i.e. >0.1mm total flame displacement) to exclude data that are susceptible to uncertainties of the flame front detection due to limited LIF *spatial* resolution. Conditional sampling on all aforementioned conditions (blue line, Fig. 6b) results in the same distribution, providing trust that the resolved s_T distribution is valid for the methodology and operating conditions.

5. Discussion

Thus far it has been shown that s_T is locally dependent along the flame surface and a large distribution exists for the operating conditions reported. The uncertainty and parameter sensitivity analyses performed provided confidence that the distribution is credible. This section presents a discussion describing the range of s_T values reported.

The distribution of s_T shown in Fig. 6 provides an ensemble-average value s_T=2.6m/s (rms=±3.8m/s and ±1.5 m/s reported uncertainty (1σ)), which is 7.2*s_L (s_L=0.36m/s at the operating conditions, [7]). Local flame instabilities caused by high pressures [13,31,32], local thermodiffusive properties [8,13], and high turbulence levels including strong flame wrinkling [1,4,9,32] are all underlying physical factors in our system that will increase s_T/s_L.

The aforementioned effects can vary locally along the flame surface, which can also lead to local situations where s_T>7.2*s_L. The large dynamic range of flame development and limited out-of-plane resolution can also result in large s_T values for the current methodology. As depicted in Figs. 4 and 5, the

flame surface is not equally transported. For the fixed Δt_{LIF} = 50μs, local flame segments drastically advance and change shape. If opposing surfaces of the flame unite (e.g. closing of concave wrinkle) the locally resolved flame progression will appear substantial and increase s_T [26]. To better resolve these effects, a large temporal dynamic range and an improved out-of-plane resolution (e.g. tri-plane, or volumetric tomography) are required.

Twenty-percent of the distribution reported in Fig. 6 contains negative displacement speeds. This occurs when local regions of the convected flame contour are transported past FS2 and the resulting flame-normal is towards the products rather than reactants. The notion of negative s_T does not pertain to rates of fuel consumption or heat release, but instead pertains to the flame displacement *relative* to the flow [27]. Although uncertainties due to limited spatial resolution or measurement precision can yield negative s_T, these occurrences still exist beyond the maximum uncertainty. Thus, negative s_T values are statistically significant (i.e. 6.5% occurrence considering 3σ uncertainty), which support findings of [2,14,15,26,27,28]. Direct numerical simulation (DNS) studies have identified three primary mechanisms attributed to negative s_T: (1) regions of high positive flame curvature exhibiting a larger diffusive flux than convective flux [27], (2) regions of high compressive and tangential strain [26], and (3) sensitivities of the prescribed isolevel (e.g. OH or fuel mass fraction) within the reaction front layer that is used to calculate local displacement speed [5,28]. In this work like other experimental investigations [14,15] no correlation is found between negative s_T and local values of flame curvature or strain. Such findings are based on the available detection system resolutions (temporal, spatial) and given operating conditions. Note that our operating conditions are quite different than the aforementioned DNS and experimental efforts, which exhibit atmospheric conditions within simpler flame-facilities. At our imaging timing, the engine operates with 12 bar, 550K unburned gas-temperature, complex flame-flow configurations, and solid boundaries – all which can lead to different mechanisms for flame transport or negative s_T.

The measurements presented are the first of its kind that quantify the distribution of local 3D flame propagation in an SI engine. They reveal the complex 3D flame transport due to advection and diffusion. Similar data processing methods are transferrable to numerical models for meaningful statistical comparisons and model development. However, the presented results demonstrate that it is important that numerical models account for negative displacement speeds such as in [27] for meaningful comparisons and further understanding of the mechanisms attributing negative s_T values. The measurements also provide an understanding of the required numerical mesh sizes needed to resolve the flame displacement speed beyond the merits of the presented work.

While these measurements provide a unique opportunity to understand flame transport in engines, they also have several shortcomings, which should be well-addressed. With the conventional lenses and cameras used, it is recognized that our detection systems under-resolve the spatial- and temporal-scales of the flame transport, which results in a *filtered* s_T value. To properly resolve local flame transport, it is recommended to resolve several measurement points within the reaction zone thickness ($\delta_L \approx 45\mu m$ at the imaging timing (1D flamelet calculations)). Improved spatial resolution in the z-direction is also required. The current experimental setup, however, vastly approached the physical limits of the conventional detection systems used and the physical space around the optical engine. Measurements and simulations with improved temporal and spatial resolution, with additional volumetric information and detection of several reaction species will provide further insight of flame transport beyond the capabilities of the presented work. Verification of such complex methodology undertaking is first intended for simpler flame-facility geometries (e.g. laminar flames or freely propagating turbulent flames as presented in [14]).

6. Conclusions

This paper describes an experimental investigation to resolve the early 3D flame propagation in a single-cylinder SI optical engine. The engine is operated at 800 RPM with premixed stoichiometric isooctane-air mixtures. Simultaneous dual-plane OH-LIF and stereoscopic PIV were used to measure the local 3D flame-normal and 3C convection velocity to resolve the local 3D flame displacement (s_T). Images were acquired 5 CA^o after spark when less than 5% of the mixture was consumed. The processing methods used to create the reconstructed 3D flame surface and extract local s_T is described. An instantaneous flame realization is shown as an example to describe the flame transport at the operating conditions. Both local s_T and convection velocity exhibit a large dynamic range and many flame-flow configurations are shown, which individually define unique flame transport along the same flame front. Thorough uncertainty and parameter sensitivity analyses performed revealed that the s_T distribution over the 80 engine cycles is credible. The distribution is centered around $s_T=7.2*s_L$ with significant regions extending both to large and negative values. Local flame instabilities caused by high in-cylinder pressures, local thermodiffusive properties, and high turbulence levels including strong flame wrinkling are underlying physical reasons for $s_T>s_L$. Occurrence of negative s_T support previous literature findings. However, under our operating conditions and filtered s_T representation, negative s_T values were not correlated with mechanisms found to cause negative s_T from previous DNS studies. For presented findings, there appears to be several physical mechanisms responsible for the large s_T distribution, which attributes to the complex nature of early flame development in SI engines. This experimental effort was the first of its kind to resolve local 3D displacement speeds in an SI engine and will be further used to study flame transport behavior for higher engine speeds and different fuel-blends. Further improvements in spatial resolution and additional volumetric information within experimental and numerical investigations will provide further insight of flame transport beyond the capabilities of the presented work.

7. Acknowledgments

The authors gratefully acknowledge financial support by the Deutsche Forschungsgemeinschaft (DFG) through PE2068 and EXC259. The authors are also especially thankful to LaVision for borrowing equipment, Dr. P.J. Trunk for providing the code and fruitful discussion, and M.-S. Benzinger (ITT, Karlsruhe) for the 1D flamelet calculations.

References

1. J.F. Driscoll, *Prog. Energy Combust. Sci.* 34 (1) (2008) 91-134
2. G. Hartung, J. Hult, R. Balachandran, M.R. Mackley, C.F. Kaminski*, Appl. Phys. B* 96 (2009) 843–862.
3. N. Chakraborty, R.S. Cant, *Proc. Combust. Inst. 32* (1) (2009) 1445–1453.
4. N. Peters, *Turbulent Combustion, Cambridge university press,* 2000.
5. Y.-C. Chen, R.W. Bilger*, Combust. Flame 131 (4) (2002) 400-435.*
6. M. Metghalchi, J.C. Keck*, Combust. Flame 48 (4) (1982) 191-210.*
7. D. Bradley, R.A. Hicks, M. Lawes, C.G.W. Sheppard, R. Woolley*, Combust. Flame, 115 (1-2) (1998) 126–144.*
8. D. Bradley, M.Z. Haq, R.A. Hicks, T. Kitagawa, M. Lawes, C.G.W. Sheppard, R. Woolley, *Combst. Flame, 133 (2003) 415-430.*
9. J.C. Keck*, Proc. Combust. Inst. 19 (1) (1982) 1451–1466.*
10. S. Jerzembeck, N. Peters, P. Pepiot-Desjardins, H. Pitch*, Combust. Flame, 156 (2009) 292-301.*
11. R. Suntz, H. Becker, P. Monkhouse, J. Wolfrum*, Appl. Phys. B 47 (4) (1988) 287-293.*
12. H. Becker, A. Arnold, R. Suntz, P. Monkhouse, J. Wolfrum, R. Maly, W. Pfister*, Appl. Phys. B 50 (6) (1990) 473-478.*
13. H. Kobayashi, Y. Kawabata, K. Maruta*, Proc. Combust. Inst. 27 (1) (1998) 941–948.*

14. P.J. Trunk, I. Boxx, C. Heeger, W. Meier, B. Böhm, A. Dreizler*, Proc. Combust. Inst. 34 (2) (2013) 3565–3572.*
15. J. Kerl, C. Lawn, F. Beyrau*, Combust. Flame 160 (2013) 2757–2769.*
16. M. Shimura, T. Ueda, G.-M. Choi, M. Tanahashi, T. Miyauchi*, Proc. Combust. Inst. 33 (1) (2011) 775-782.*
17. D.A. Knaus, F.C. Gouldin, D.C. Bingham*, Combust. Sci. Technol. 174 (1) (2002) 101-134.*
18. J.R. Ault, P.O. Witze*, SAE Technical Paper 981427 (1998).*
19. C. Mounaïm-Rousselle, L. Landry, F. Halter, F. Foucher*, Proc. Combust. Inst. 34 (2) (2013) 2941-2949.*
20. B. Peterson, D.L. Reuss, V. Sick, *Combust. Flame* 161 (2014) 240-255.
21. E. Baum, B. Peterson, B. Böhm, A. Dreizler*, Flow Turb. Combust. 92(1-2) (2014) 269-297.*
22. M. Desbrun, M. Mayer, P. Schröder. A.H. Barr*, Proc. Conf. Comp. Graphics Interactive Tech., ACM Press/Addison-Wesley Publishing, New York, 1999, p. 317-324.*
23. L. Piegle, *IEEE 11 (1) (1991) 55-71.*
24. J. Weickert*, Anisotropic Diffusion in Image Processing, Teubner Verlag, Stuttgart, 1998.*
25. U. Maas, J. Warnatz*, Combust. Flame 74 (1988) 53-69.*
26. J.H. Chen, H.G. Im*, Proc. Combust. Inst. 27 (1) (1998) 819–826.*
27. I.R. Gran, T. Echekki, J.H. Chen*, Proc. Combust. Inst. 26 (1) (1996) 323–329.*
28. S.H. Kim, R.W. Bilger, CTR Annual Report, 2005.
29. G.P. Beretta, M. Rashidi, J.C. Keck*, Combst. Flame 52 (1) (1983) 217-245.*
30. N.J. Lawson, J. Wu*, Meas. Sci. Tech. 8 (12) (1997) 1455–1464.*
31. C.K. Law, G. Jomaas, J.K. Bechtold*, Proc. Combust. Inst. 30 (2005) 159-167.*
32. D. Bradley, M. Lawes, C.G.W. Sheppard*, Proc. Inst. Mech. Engineer 214 (1) (2000) 257-268.*

Table 1:

Engine details and operating conditions

Engine speed	800RPM
Intake press., temp.	0.95bar, 300K
Fuel, amount (PFI)	C_8H_{18}, 27.4mg/cycle
Eqivalence ratio	1.0
Spark timing, dwell	19°bTDC, 3.5ms
IMEP, COV	5.1 bar, 1.1%

Lines: 8

Column: Single column

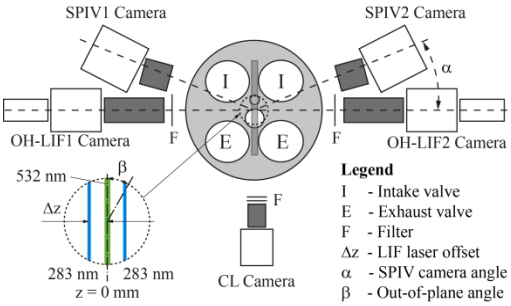

Figure 1: Experimental setup of multi-plane detection in engine.

Column: Single column
Color: b/w

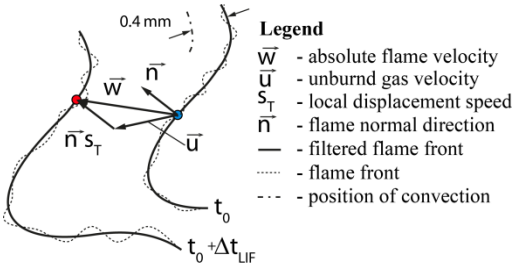

Figure 2: Vectorial schematic of local transport of flame surface.

Column: Single column
Color: b/w

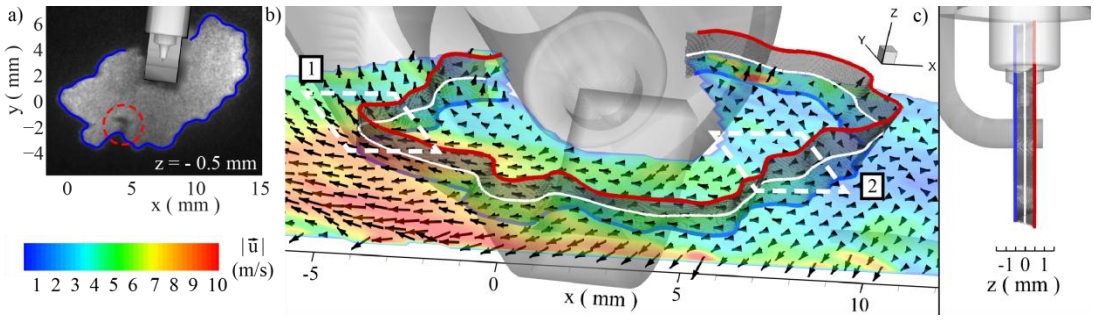

Figure 3: Instantaneous realization of flame. (a) Raw LIF-image and reaction-zone (blue line). Red-circle highlights unresolved wrinkle. (b) 3D flame surface imposed onto 3C flow-field (every 4th vector) at t_0, (c) side-view of 3D flame surface. Rectangles 1 and 2 highlight flame segments described in Fig. 5.

Column: Double column
Color: RGB

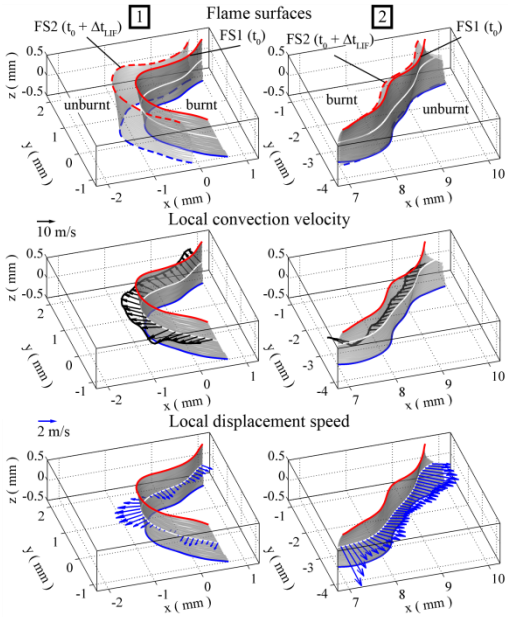

Figure 4: Flame segments 1 and 2 highlighted in Fig. 3 to describe individual components of flame transport. (Top) FS1 and FS2, (middle) convection of SPIV flame contour, (bottom), s_T superimposed onto FS1.

Column: Single column
Color: RGB

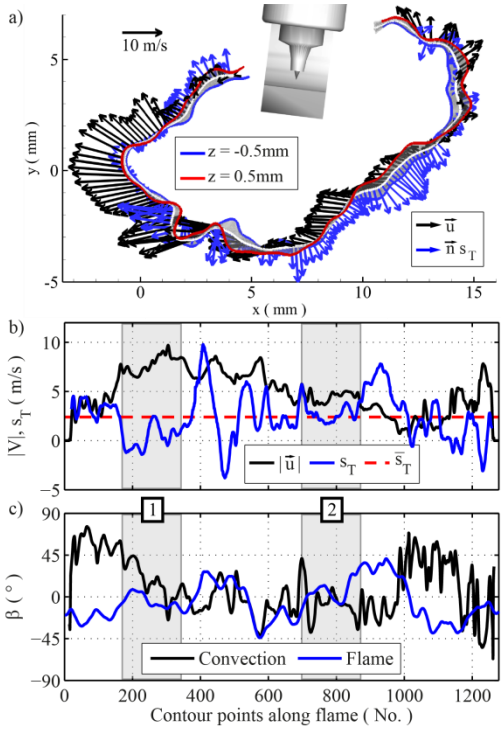

Figure 5: (a) s_T (blue) and convection velocity (black) along flame surface, (b) local velocity values along flame contour, (c) local out-of-plane flame- and convection-angle. Shaded regions correspond to flame segments shown in Fig. 5. Red line indicates cycle-average s_T.

Column: Single column
Color: RGB

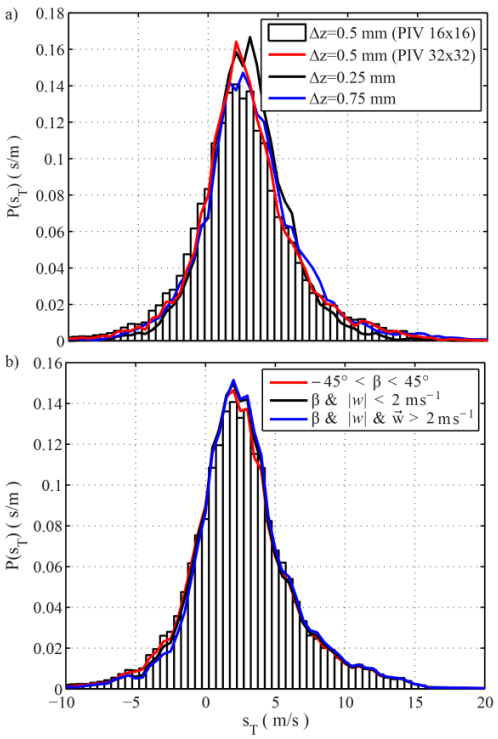

Figure 6: Sensitivity of s_T-calculation on input parameters. (a) original s_T PDF (bars) compared to PDFs using different PIV resolution (red) and experiments utilizing Δz=0.25, 0.75mm (black, blue), (b) original s_T PDF (bars) compared to PDFs that are conditionally sampled accounting for out-of-plane convection angles -45<β<45 (red), out-of-plane convection velocity |w|<2m/s (black) and absolute displacement *w*>2m/s (blue).

Column: Single column
Color: RGB

Figure 1: Experimental setup of multi-plane detection in engine.

Figure 2: Vectorial schematic of local transport of flame surface.

Figure 3: Instantaneous realization of flame. (a) Raw LIF-image and reaction-zone (blue line). Red-circle highlights unresolved wrinkle. (b) 3D flame surface imposed onto 3C flow-field (every 4^{th} vector) at t_0, (c) side-view of 3D flame surface. Rectangles 1 and 2 highlight flame segments described in Fig. 5.

Figure 4: Flame segments 1 and 2 highlighted in Fig. 3 to describe individual components of flame transport. (Top) FS1 and FS2, (middle) convection of SPIV flame contour, (bottom), s_T superimposed onto FS1.

Figure 5: (a) s_T (blue) and convection velocity (black) along flame surface, (b) local velocity values along flame contour, (c) local out-of-plane flame- and convection-angle. Shaded regions correspond to flame segments shown in Fig. 5. Red line indicates cycle-average s_T.

Figure 6: Sensitivity of s_T-calculation on input parameters. (a) original s_T PDF (bars) compared to PDFs using different PIV resolution (red) and experiments utilizing Δz=0.25, 0.75mm (black, blue), (b) original s_T PDF (bars) compared to PDFs that are conditionally sampled accounting for out-of-plane convection angles $-45<\beta<45$ (red), out-of-plane convection velocity $|w|<2$m/s (black) and absolute displacement $w>2$m/s (blue).